McMaster University
DigitalCommons@McMaster

Open Access Dissertations and Theses | Open Dissertations and Theses

10-1-2011

A Semi-Definite, Nonlinear Model for Optimizing k-Space Sample Separation in Parallel Magnetic Resonance Imaging

Qiong Wu
McMaster University, wuq29@mcmaster.ca

Follow this and additional works at: http://digitalcommons.mcmaster.ca/opendissertations

Part of the Biological Engineering Commons, and the Computational Engineering Commons

Recommended Citation
Wu, Qiong, "A Semi-Definite, Nonlinear Model for Optimizing k-Space Sample Separation in Parallel Magnetic Resonance Imaging" (2011). *Open Access Dissertations and Theses.* Paper 5524.

This Thesis is brought to you for free and open access by the Open Dissertations and Theses at DigitalCommons@McMaster. It has been accepted for inclusion in Open Access Dissertations and Theses by an authorized administrator of DigitalCommons@McMaster. For more information, please contact scom@mcmaster.ca.

A Semi-Definite, Nonlinear Model for Optimizing k-Space Sample Separation in Parallel Magnetic Resonance Imaging

A Semi-Definite, Nonlinear Model for Optimizing k-Space Sample Separation in Parallel Magnetic Resonance Imaging

By
Qiong Wu B.Eng.

A Thesis
Submitted to the School of Graduate Studies
in Partial Fulfillment of the Requirements
for the Degree
Master of Applied Science

McMaster University
© Copyright by Qiong Wu, July 21, 2011

MASTER OF APPLIED SCIENCE(2011) McMaster University
BIOMEDICAL ENGINEERING Hamilton, Ontario

TITLE: A Semi-Definite, Nonlinear Model for Optimizing k-Space Sample Separation in Parallel Magnetic Resonance Imaging

AUTHOR: Qiong Wu B.Eng.(Southern Medical University)

SUPERVISOR: Dr. Christopher K. Anand

NUMBER OF PAGES: xi, 42

LEGAL DISCLAIMER: This is an academic research report. I, my supervisor, defence committee, and university, make no claim as to the fitness for any purpose, and accept no direct or indirect liability for the use of algorithms, findings, or recommendations in this thesis.

Abstract

Parallel MRI, in which k-space is regularly or irregularly undersampled, is critical for imaging speed acceleration. In this thesis, we show how to optimize a regular undersampling pattern for three-dimensional Cartesian imaging in order to achieve faster data acquisition and/or higher signal to noise ratio (SNR) by using nonlinear optimization. A new sensitivity profiling approach is proposed to produce better sensitivity maps, required for the sampling optimization. This design approach is easily adapted to calculate sensitivities for arbitrary planes and volumes. The use of a semi-definite, linearly constrained model to optimize a parallel MRI undersampling pattern is novel. To solve this problem, an iterative trust-region is applied. When tested on real coil data, the optimal solution presents a significant theoretical improvement in accelerating data acquisition speed and eliminating noise.

Acknowledgments

I would like to thank my supervisors Dr. Christopher K. Anand for his patient guidance and wonderful support throughout my degree. Thanks to Dr. Anand in particular for offering me plenty of opportunities discussing my research at many conferences and workshops.

I would also like to express my sincere thanks to Dr. Michael D. Noseworthy for his excellent course in medical imaging which provided me a broad view of medical imaging field and his generous help in my research and career.

I thank all members in our research group, particularly Zhenghua Nie, Anuroop Sharma, for their friendly help during me graduate study and for the pleasant and exciting working environment we have established.

I would also like to express my greatest thanks to my parents, family and friends for their support and encouragement.

Contents

Abstract **iii**

Acknowledgments **v**

List of Figures **ix**

List of Tables **xi**

1 Introduction **1**

2 SENSE Imaging Backgrounds **3**
2.1 MRI Basics 3
2.2 SENSE imaging 5

3 Sensitivity Estimation **9**
3.1 Polynomial Fitting Models 9
3.1.1 Ordinary Polynomial Fitting 10
3.1.2 Rational Polynomial Fitting 11
3.2 Polynomial Basis Selection 12
3.2.1 Orthogonal Ordinary Polynomial Basis 12
3.2.2 Weighted Othonormal Ordinary Polynomial Basis . . . 13
3.2.3 Legendre Polynomial Basis 13
3.3 Results and Discussion 14
3.3.1 Phantom Results 14
3.3.2 Brain Data Results 19

4 Undersampling Optimization **21**
4.1 Semi-definite Optimization Model 21
4.2 Encoding Matrix Simplification 22
4.3 Modified Model with Linear Constraints 24

5 Trust-Region Method **25**
5.1 Trust-Region Method 25
5.2 SDP Reformulation 26

6 Results **31**
6.1 Phantom Simulation 31
6.2 Phantom Simulation with Larger FOV 33

7 Conclusion **39**
7.1 Sensitivity Profiling 39
7.2 SDP Model 40

A Relation of Transformations Between Image Domain and K-space **41**

List of Figures

2.1 a) Three dimensional phase encoding imaging sequence; b) effects of the sequence in data sampling in k-space. 4

2.2 Aliasing due to undersampling: red and green curves show two continuous functions representing the signal produced by single points in k-space, and the identical discrete samples for both in blue in (a).In (b) we see the corresponding image-space representations of the true signals (red and green delta functions), and the reconstructed signal in blue showing very significant aliasing. 5

3.1 Interpolated Sensitivity in Different Models: upper row is from ordinary fitting model and lower row is from rational fitting model. 15

3.2 Reconstructed Images in Different Models: (a) ordinary polynomial fitting model, (b) rational polynomial fitting model. . . 15

3.3 Sensitivity with Different Polynomial Bases: (a) orthogonal polynomial basis, (b) cylinder-weighted orthogonal polynomial basis, (c) body image-weighted orthogonal polynomial basis, (d) Legendre polynomial basis. 16

3.4 Reconstructed Image with Different Polynomial Bases: (a) orthogonal polynomial basis, (b) cylinder-weighted orthogonal polynomial basis, (c) body image-weighted orthogonal polynomial basis, (d) Legendre polynomial basis. 17

3.5 Reconstructed Image with Different Orders of Polynomial Basis:(a)-(d) Legendre polynomials of order 6 to 9 from right to left. (e)-(h) Orthonormal polynomials of order 6 to 9 from right to left. 17

3.6 (a) reconstructed brain image using the sensitivity profiling calculated from the proposed approach; (b) reconstructed brain image using the sensitivity calculated based on assumption that $\sqrt{\sum I^{h^2}}$ is body coil data. 19

6.1 Optimal undersampling patterns in image space (a,d), and k-space (b,e) and reconstructed images (c,f). Red arrows show initial aliasing vectors; blue arrows show optimal aliasing vectors pattern; red dots show the initial aliased point set; blue dots show optimal aliased sets; green lines are the linear constraints in the SDP model. Case 1: (a,b,c). Case 2: (d,e,f). . . 33

6.2 Rounded optimal (a) and regular (e) sampling patterns; corresponding reconstructed images without (b,e), and with (c,f) additional noise. 34

6.3 Optimal undersampling patterns in image space (a,d), and k-space (b,e) and reconstructed images (c,f), using 4X FOV data to reduce the loss of efficiency from rounding. Red arrows show initial aliasing vectors; blue arrows show optimal aliasing vectors pattern; red dots show the initial aliased point set; blue dots show optimal aliased sets; green lines are the linear constraints in the SDP model. Case 3: (a,b,c). Case 4: (d,e,f). . . 35

6.4 Reconstructed Image with Different Levels of Noise: the upper row is based on the optimal subsampling pattern; the lower on the regular subsampling pattern. (a)(f) undersampling pattern in k-space, (b)(g) without noise, (c)(h) 1% noise, (d)(i) 5% noise, (e)(j) 20% noise. 36

6.5 Reconstruction errors as a function of added noise. 37

List of Tables

3.1 Computation time with different polynomial orders (sec) using MATLAB R2010a installed on a 2.6GHz dual-core AMD Opteron processor. 18

6.1 Numerical Result of Optimal Undersampling Vectors 32
6.2 Numerical Result of Optimal Undersampling Vector 34

Chapter 1

Introduction

Magnetic Resonance Imaging (MRI) is a widely used clinical imaging technology. Compared to CT and X-Ray, MRI is non-invasive, uses non-ionizing radiation and able to generate multiple image contrasts. Nowadays, MRI can produce excellent anatomic images with sub-milimetre resolution. In addition to anatomical information, MRI is becoming a valuable tool for monitoring dynamic physiologic processes including function and perfusion. Moreover, MRI is widely used in cardiac diagnosis and metabolism analysis. However, the speed of data collection of conventional MRI techniques is inherently limited due to the essentially sequential fashion of collecting data by successive gradient encoding[13]. Besides gradient performance enhancement to accelerate data acquisition, parallel sensitivity encoding (SENSE) techniques employ multiple surface-coil or phased-array detectors to further accelerate MRI data collection [14]. Parallel MRI provides manifold increases in imaging speed by replacing some of the gradient spatial-encoding steps with spatial information derived from the distinct sensitivity profiles of the array coils[3].

In this thesis, we show how to optimize a regular undersampling pattern for three-dimensional Cartesian imaging in order to achieve faster data acquisition and/or higher signal to noise ratio (SNR) by using nonlinear optimization. In Chapter 3, we propose a new sensitivity profiling approach to produce better sensitivity maps, required for the sampling optimization. This design approach is easily adapted to calculate sensitivities for arbitrary planes and volumes.

The use, in Chapter 4, of a semi-definite, linearly constrained model to optimize a parallel MRI undersampling pattern is novel, and the main contribution of this thesis. To solve this problem, an iterative trust-region method

is applied. When tested on real coil data, the optimal solution presents a significant theoretical improvement in accelerating data acquisition speed and eliminating noise. The thesis contains five chapters with three topics, namely, sensitivity profiling, undersampling optimization, and the trust-region method.

All data was collected on a 1.5T engineering prototype scanner, using an 8 channel head coil, and integrated body coil.

Chapter 2

SENSE Imaging Backgrounds

2.1 MRI Basics

The clinical use of Magnetic Resonance Imaging (MRI) is based on the observation of water molecules (in particular, of hydrogen) in the human body. In summary, an MRI experiment can be described as follows: upon the application of an external static magnetic field, the protons of water molecules will be preferentially aligned with the magnetic field as magnetic dipoles. When they are disturbed by a second alternating magnetic field of induction at a certain radio frequency, they begin to resonate. According to Faraday's law, the precessing of magnetic dipoles induces an electric current, giving rise to a signal, in a RF receive coil surrounding them. The signal is detected in the radio frequency (RF) range, but transformed into the lower audio frequency range for sampling and analysis[9, 6].

The spatial distribution of protons can be encoded into the signals by the application of linear magnetic field gradients $\boldsymbol{G}$. This is usually understood in terms of the concept of k-space. The gradients $\boldsymbol{G}$ correlate the precessional frequency $\boldsymbol{k}$ with spatial position, measured in coordinates, $\boldsymbol{r}$,

$$\boldsymbol{k} = \int_0^t \boldsymbol{G}(\boldsymbol{r}, \tau) d\tau$$

whereas the signal intensity $M(\boldsymbol{k})$, considered as a complex value $M = M_x + iM_y$, has magnitude proportional to the proton density weighted $|\rho(\boldsymbol{r})|$ in tissues and decays with their relaxation times (T_1, T_2, and T_2^*). The complex phase of ρ encodes susceptibility and other effects which are outside the scope of this thesis. MRI scan can be applied both in 2D and 3D and most of the

discussion in thesis is based on a 3D example. The dominating schemes for MRI have been based on the Fourier transform relationship between k-space

$$\{M(\boldsymbol{k})|M \in \mathbb{C}, \boldsymbol{k} \in \mathbb{R}^3\}$$

and image space

$$\{\rho(\boldsymbol{k})|\rho \in \mathbb{C}, \boldsymbol{r} \in \mathbb{R}^3\}.$$

In the mathematical point of view, the MR signal received, when neglecting all relaxation phenomena, can be written as:

$$M_\kappa(\boldsymbol{k}) = \mathcal{F}\{\rho(\boldsymbol{r})\} = \int_{\mathbb{R}^3} \rho(\boldsymbol{r}) e^{j\boldsymbol{k}_\kappa \cdot \boldsymbol{r}} d\boldsymbol{r} \tag{2.1}$$

In the case of pulsed RF excitation, the Fourier transform is used to extract the frequency and intensity information, resulting in MR images. To generate conventional multidimensional images, k-space is sampled by the use of incremental phase encoding in the absence of RF pulses[16]. The gradient fields $\boldsymbol{G}$ directly manipulate the $\rho(\boldsymbol{r})$ to be depicted. Since each line of k-space corresponding to a certain proton magnetization requires preparation time (including RF pulses and delays), serial imaging is time consuming. As a consequence only one such encoding can be performed at a time, resulting in the long scan durations that severely restricts the application of MRI[12], see in Figure 2.1.

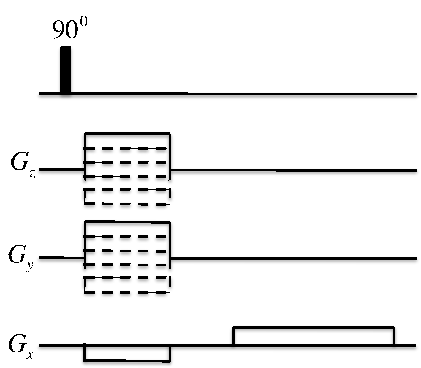

Figure 2.1: Three dimensional gradient echo with phase encoding in y and z directions.

2.2 SENSE imaging

In order to accelerate imaging speed, parallel imaging techniques have been proposed[8, 4, 10, 17]. Different from conventional MRI, receive coils for parallel imaging techniques consist of a number of elements or channels, each working more or less independently and sensitizing to a different region of the field of view (FOV). The coils generally work in combination with a separate, larger transmit coil with uniform excitation profile over the entire FOV. In general, by reducing the encoding steps by a factor of L, the L-folded image is obtained. A 1D example of aliasing is shown in Figure 2.2.

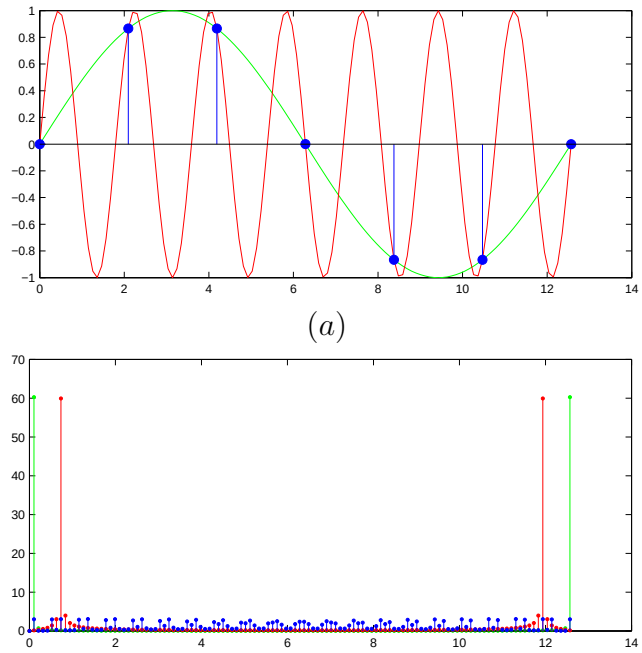

Figure 2.2: Aliasing due to undersampling: red and green curves show two continuous functions representing the signal produced by single points in k-space, and the identical discrete samples for both in blue in (a).In (b) we see the corresponding image-space representations of the true signals (red and green delta functions), and the reconstructed signal in blue showing very significant aliasing.

As early as 1993, Ra and Rim described a method that uses sets of equally spaced k-space lines from multiple receiver coils and combines them with sensitivity profile information in order to remove the aliasing that occurs

due to the undersampling. A 4-folded decrease in the image acquisition time of a water phantom was shown using an array of four coils[7, 15]. Later on, the sensitivity encoding (SENSE) method was proposed by Pruessmann et al., which is a parallel imaging technique relying on the use of 2D sensitivity profile information in order to reduce image acquisition times in MRI[14]. The Cartesian version of SENSE requires the acquisition of equally spaced k-space lines in order to reconstruct sensitivity weighted, aliased versions of the image. The aliasing is then removed with the use of the sensitivity profile information at each pixel. This is done by resolving in the space domain the linear system of equations obeyed by the intensity of each pixel in the image.

In the mathematical point of view, SENSE imaging can be modeled as a linear system as follows,

$$M_{c,\kappa}(\boldsymbol{k}) = \mathcal{F}_s\{\rho(\boldsymbol{r})\} = \int_{\mathbb{R}^3} \rho(\boldsymbol{r}) S_c(\boldsymbol{r}) e^{j\boldsymbol{k}_\kappa \cdot \boldsymbol{r}} d\boldsymbol{r} \tag{2.2}$$

where $\mathcal{F}_s$ represents the hybrid encoding functions, which are no longer pure plane waves $\mathcal{F}$ in Eq. 2.1, but plane waves multiplied by coil sensitivity $S_c(\boldsymbol{r})$. Accordingly, in their equivalent k-space representation they are no longer Dirac peaks but now have distinct shapes and a significant extent. Mathematically speaking, this is the result of a convolution with the Fourier transform of the respective coil sensitivity function.

Based on this observation, the Fourier representations of the coil sensitivities may also be referred to as the coils k-space kernels. The most important aspect of the transition to hybrid encoding functions is that different coils have different sensitivities and hence different k-space kernels. This means that, with multiple receiver coils, one can perform multiple different encodings at one time. Owing to the extent of these kernels, each encoding no longer yields a genuine k-space sample but rather a weighted integral of data from a certain k-space neighborhood. Therefore the encoding operation can no longer be interpreted as sampling the Fourier transform of $\rho(\boldsymbol{r})$. In a more general mathematical sense the integral in Eq. 2.2 represents a scalar product, which may be interpreted as the projection of $\rho(\boldsymbol{r})$ onto the hybrid encoding basis $E_{c,\kappa}(\boldsymbol{r}, \boldsymbol{k})$,

$$M_{c,\kappa}(\boldsymbol{k}) = \mathcal{F}_s\{\rho(\boldsymbol{r})\} = \int_{\mathbb{R}^3} \rho(\boldsymbol{r}) E_{c,\kappa}(\boldsymbol{r}, \boldsymbol{k}) d\boldsymbol{r}$$

where $E_{c,\kappa}(\boldsymbol{r})$ is defined as follows,

$$E_{c,\kappa}(\boldsymbol{r}, \boldsymbol{k}) = S_c(\boldsymbol{r}) e^{j\boldsymbol{k}_\kappa \boldsymbol{r}}$$

As a consequence, image reconstruction can no longer be accomplished by mere Fourier transform but amounts to recovering $\rho(\boldsymbol{r})$ from a set of more general projections[12].

In order to appropriately cover the k-space of the image $\rho(\boldsymbol{r})$, which $\rho(\boldsymbol{r})$ is the reconstructed image, the choice of the phase modulations used in the inversion matrix should be determined by the frequency content of the sensitivity profile. In the spatial domain, the image received in a coil having a sensitivity profile $S_c(\boldsymbol{r})$ can be written as follows,

$$I_c(\boldsymbol{r}) = S_c(\boldsymbol{r})\rho(\boldsymbol{r})$$

In the frequency domain, the k-space profile of $I_c(\boldsymbol{r})$ is shown as follows,

$$M_c(\boldsymbol{k}) = \hat{S}_c(\boldsymbol{k}) * M(\boldsymbol{k})$$

where $*$ is convolution operator, $M(\boldsymbol{k})$ is the k-space profile of the image $\rho(\boldsymbol{r})$, $\hat{S}_c(\boldsymbol{k})$ is the k-space profile of the sensitivity profile $S_c(\boldsymbol{r})$. This convolution amounts to a blurring of the k-space data $M(\boldsymbol{k})$ of the image. Since a different convolution is performed for each coil, a different blurring of $M(\boldsymbol{k})$ occurs at each coil. Subsampling the convolved k-space data received in different coils therefore results in different coverages of the k-space of the image $\rho(\boldsymbol{k})$. Hence, in order to get the best k-space coverage of the $\rho(\boldsymbol{r})$ for a given $S_c(\boldsymbol{r})$, it is necessary to optimally sample the k-space data from all the coils[7].

Moreover, simultaneous encoding by coil sensitivity can be used to complement gradient encoding and hence to reduce the number of gradient-encoding steps required for one image. It is an important and as yet largely unanswered question how the reduced set of sampling positions in k-space can be optimally chosen. Various undersampling patterns have been investigated. In terms of sampling trajectory, k-space sampling strategies can be categorized into two main approaches, Cartesian and non-Cartesian sampling. Cartesian undersampling regularly or irregularly undersamples k-space in phase encoding direction(s). Based on the redundant information from multiple coils, the image can be reconstructed with regularization. Cartesian undersampled image reconstruction is relatively cheap in computation but misses amount of spatial information, especially regularly sampled k-space data could miss the middle of k-space, resulting in poor contrast resolution. Compared with Cartesian

undersampling, non-Cartesian sampling is more versatile and faster in data acquisition, but the reconstruction is fairly expensive and gridding in k-space may also cause unpredictable artifacts which are difficult to eliminate in post processing.

Chapter 3

Sensitivity Estimation

In SENSE imaging, sensitivity profiles of RF receive coils are required to reconstruct images. Obtaining the sensitivity information in a clinical setting has been proven problematic[18]. To calculate these profiles, a number of techniques described in the literature can be used[13, 7, 18]. In all of these methods, as is common in the literature, it is assumed that the sum of squares image obtained from all receive coils is equivalent to the body image. However, most of the receive coils are surface coils, which have low signals in the center of the object being imaged. As a result, the sum of squares image is non-homogeneous. Sensitivities calculated based on this assumption produce non-homogeneous images, which are of less clinical use, because they take longer to adjust (window and level).

In this section, different from the previous approaches, a newly developed sensitivity profiling approach has been proposed, followed by topics on: introduction of polynomial fitting models, polynomial basis selection, and results and discussion.

3.1 Polynomial Fitting Models

As discussed in Chapter 2, the sensitivity of a receiver coil S_c is determined by the Biot-Savart Law and the principle of reciprocity. Specifically, $S_c(\boldsymbol{r})$ is the laboratory frame magnetic field at location $\boldsymbol{r}$ produced by a hypothetical unit current flowing in the coil. However, even in the low frequency limit, it is impractical to calculate $S_c(\boldsymbol{r})$ directly by Biot-Savart Law explicitly, because it is highly dependant on coil geometry, position, orientation, coil load, and the scan object.

As an alternative, the sensitivity profile can be estimated from reconstructed images. Using polynomials to fit sensitivity has been used in parallel imaging for many years[14, 7]. All of the previous sensitivity models use the sum-of-squares image in place of a uniform (body coil) image. As discussed at the beginning of this chapter, this assumption will lead to low signal in the centre of objects. To overcome this disadvantage, we propose the following sensitivity profiling scheme, a set of relatively low resolution fully sampled images are acquired by a body coil and multiple surface coils. More specifically, image $I^b(\boldsymbol{r})$ is the image from the body coil, which we assume to have a homogeneous sensitivity profile covering the whole object. This is reasonable for low field imaging. Image $I_c^h(\boldsymbol{r})$ is the image of the same object acquired using the cth surface coil, which is only sensitive to part of the object. With the low resolution of body coil image and surface coil images, polynomials are fit to them and the coefficients of polynomials can easily be calculated. Based on the set of coefficients, interpolation of the RF receive coils sensitivity is applied. The polynomials are then interpolated to the resolution required for subsequent SENSE reconstruction resolutions and geometries. This designed calculation is chosen for its simplicity and adaptability to 3D applications. Furthermore, both the ordinary polynomial fitting and rational polynomial fitting are investigated.

3.1.1 Ordinary Polynomial Fitting

$S_c(\boldsymbol{r})$ is the sensitivity profile of the cth surface coil and can be represented by a polynomial,

$$S_c(\boldsymbol{r}) = \sum_i a_{i,c} p_i(\boldsymbol{r})$$

$\{\boldsymbol{p}_i\}$ is the polynomial basis for sensitivity fitting. Without consideration of noise in images,

$$I_c^h(\boldsymbol{r}) = I^b(\boldsymbol{r}) S_c(\boldsymbol{r})$$

. Moreover, we assume only the information from the object (and not noisy signal from the surrounding air) contributes to polynomial fitting. Among various approaches which can be utilized to detect the object region, the magnitude of the body image is a good choice as weighting W, because it is easy to measure, relatively cheap in computation, as well as rich in region information. As a result, weighting W is introduced as follows,

$$W = \sqrt{I^b \cdot_{\text{pointwise}} I^{b*}}$$

. To sum up, the coefficients can be calculated as follows,

$$\min_{a_{i,c}} \sum_{\boldsymbol{r}\in\{\text{voxel locations}\}} \|I^b(\boldsymbol{r})S_c(\boldsymbol{r}) - I_c^h(\boldsymbol{r})\|^2 W(\boldsymbol{r}) \tag{3.1}$$

where

$$S_c(\boldsymbol{r}) = \sum_i a_{i,c} p_i(\boldsymbol{r}).$$

3.1.2 Rational Polynomial Fitting

As metioned at the begining of this section, the sensitivity profile is the laboratory frame magnetic field produced by a hypothetical unit direct current flowing in the coil. Based on Biot-Savart law,

$$S_c(\boldsymbol{r}) = \int_{\mathbb{R}^3} \frac{\mu_0}{4\pi} \frac{\boldsymbol{I} d\boldsymbol{I} \times \boldsymbol{r}}{|\boldsymbol{r}|^3} \tag{3.2}$$

where $\boldsymbol{I}$ is the current, $d\boldsymbol{I}$ is a vector, whose magnitude is the length of the differential element of the wire, and whose direction is the direction of conventional current, S_c is the sensitivity profile, μ_0 is the magnetic constant, $\boldsymbol{r}$ is the full displacement vector from the wire element to the point, where we want to get the sensitivity.

Based on Eq. 3.2, when $\boldsymbol{r}$ goes to $\mathbf{0}$, S_c would go to infinity. In other words, the sensitivity profile of the area which is close to surface coil wire will go to infinity. In mathematical point of view, the points in the area are poles of the function $S_c(\boldsymbol{r})$. To model this sigularity property, a rational polynomial fitting model is investigated. Different from the ordinary polynomial, $S_c(\boldsymbol{r})$ can be modeled as the fraction of two polynomials $S_{p,c}(\boldsymbol{r})$, $S_{q,c}(\boldsymbol{r})$. The same weighting is applied to this model,

$$\min_{a_{i,c},b_{i,c}} \sum_{\boldsymbol{r}\in\{\text{voxel locations}\}} \|I^b(\boldsymbol{r})S_{p,c}(\boldsymbol{r}) - I_c^h(\boldsymbol{r})S_{q,c}(\boldsymbol{r})\|^2 W(\boldsymbol{r}) \tag{3.3}$$

where

$$\begin{aligned} S_{p,c}(\boldsymbol{r}) &= \sum_i a_{i,c} p_i(\boldsymbol{r}) \\ S_{q,c}(\boldsymbol{r}) &= \sum_j b_{j,c} q_j(\boldsymbol{r}) \\ S_c(\boldsymbol{r}) &= \frac{S_{p,c}(\boldsymbol{r})}{S_{q,c}(\boldsymbol{r})} \end{aligned}$$

3.2 Polynomial Basis Selection

In the above models Eq. 3.1 or Eq. 3.3, both objective functions are quadratic. Based on numerical optimization theory, when $f : \mathbb{R}^m \to \mathbb{R}$ is twice continuously differentiable and the Hessian $\nabla^2 f$ is invertible, both of the problems can be solved with one step of Newton's method[5]. Take Eq. 3.1 for example, objective function in the ordinary polynomial fitting is shown below,

$$f(a_1, a_2, \cdots, a_m) = \sum_{\boldsymbol{r} \in \{\text{position locations}\}} \|I^b(\boldsymbol{r})S_c(\boldsymbol{r}) - I_c^h(\boldsymbol{r})\|^2 W(\boldsymbol{r})$$

Consequently, the Hessian of f is calculated as follows,

$$\frac{\partial^2 f}{\partial a_i \partial a_j} = \int_{\boldsymbol{r}} 2 w_{\boldsymbol{r}} {i_{\boldsymbol{r}}^b}^2 p_i(\boldsymbol{r}) p_j(\boldsymbol{r})$$

define $\langle \boldsymbol{p}_i, \boldsymbol{p}_j \rangle_{w'} = \int_{\boldsymbol{r}} 2 w_{\boldsymbol{r}} {i_{\boldsymbol{r}}^b}^2 p_i(\boldsymbol{r}) p_j(\boldsymbol{r})$, Hessian of f can be written as follows,

$$H = \begin{pmatrix} \langle\langle \boldsymbol{p}_1, \boldsymbol{p}_1 \rangle_{w'} & \langle \boldsymbol{p}_1, \boldsymbol{p}_2 \rangle_{w'} & \cdots & \langle \boldsymbol{p}_1, \boldsymbol{p}_m \rangle_{w'} \\ \langle\langle \boldsymbol{p}_2, \boldsymbol{p}_1 \rangle_{w'} & \langle \boldsymbol{p}_2, \boldsymbol{p}_2 \rangle_{w'} & \cdots & \langle \boldsymbol{p}_2, \boldsymbol{p}_m \rangle_{w'} \\ \vdots & \vdots & \ddots & \vdots \\ \langle\langle \boldsymbol{p}_m, \boldsymbol{p}_1 \rangle_{w'} & \langle \boldsymbol{p}_m, \boldsymbol{p}_2 \rangle_{w'} & \cdots & \langle \boldsymbol{p}_m, \boldsymbol{p}_m \rangle_{w'} \end{pmatrix} \tag{3.4}$$

In order to solve the above problem, the square matrix H must be numerically invertible. In other words, the columns of the matrix are supposed to be linear independent. Consequently, polynomial basis selection is critical in solving the problem. Based on the discussion above, two criteria need to be considered in selection of polynomial basis: $\{\boldsymbol{p}_i\}$ is linear independent, as well as combination of $\{\boldsymbol{p}_i\}$ smooth enough to map smoothness of sensitivity. In this section, we will discuss three polynomial bases that were used in this fitting problem.

3.2.1 Orthogonal Ordinary Polynomial Basis

In various polynomial basis, $\{x^i y^j z^k\}$ is the easiest one to calculate, where (x, y, z) are the coordinates of $\boldsymbol{r}$ in space. However, $\{x^i y^j z^k\}$ cannot be directly used in our models because the polynomials are highly linear dependent. To modify our polynomial basis set, Gram-Schmidt orthonormalization is applied. Define a set of polynomials $\{p_m(\boldsymbol{r}) | p_m(\boldsymbol{r}) = x^i y^j z^k, -1 \leq x, y, z \leq 1\}$. Define

the inner product $\langle \boldsymbol{p}, \boldsymbol{q} \rangle = \int_{\boldsymbol{r}} p(\boldsymbol{r}) q(\boldsymbol{r}) d\boldsymbol{r}$, the Gram-Schmidt process is

$$\begin{aligned} \boldsymbol{p}'_0 &= \boldsymbol{p}_0 \\ \boldsymbol{p}'_1 &= \boldsymbol{p}_1 - \frac{\langle \boldsymbol{p}'_0, \boldsymbol{p}_1 \rangle}{\langle \boldsymbol{p}'_0, \boldsymbol{p}'_0 \rangle} \boldsymbol{p}'_0 \\ \boldsymbol{p}'_2 &= \boldsymbol{p}_2 - \frac{\langle \boldsymbol{p}'_0, \boldsymbol{p}_2 \rangle}{\langle \boldsymbol{p}'_0, \boldsymbol{p}'_0 \rangle} \boldsymbol{p}'_0 - \frac{\langle \boldsymbol{p}'_1, \boldsymbol{p}_2 \rangle}{\langle \boldsymbol{p}'_1, \boldsymbol{p}'_1 \rangle} \boldsymbol{p}'_1 \\ &\cdots \end{aligned} \tag{3.5}$$

Notice Eq. 3.5 is not a complete Gram-Schmidt procedure, because it omits the normalization process. The reason for that is because the Gram-Schmidt procedure is highly expensive and our goal is to make the Hessian of f invertible. Orthogonalization is good enough to satisfy our requirements.

3.2.2 Weighted Othonormal Ordinary Polynomial Basis

Besides the ordinary orthogonal polynomial basis, we also investigated a weighted orthogonal polynomial basis set. Based on the observation of Eq. 3.4, we defined a weighted Gram-Schmidt process. Similar procedure to Eq. 3.5, we used weighted inner product $\langle \boldsymbol{p}, \boldsymbol{q} \rangle_w$ instead of $\langle \boldsymbol{p}, \boldsymbol{q} \rangle$ when calculating the projection,

$$\langle \boldsymbol{p}_i, \boldsymbol{p}_j \rangle_w = \int_{\boldsymbol{r}} w_{\boldsymbol{r}} p_i(\boldsymbol{r}) p_j(\boldsymbol{r}) \tag{3.6}$$

Regarding to choice of $w_{\boldsymbol{r}}$, $W = \sqrt{I^b \cdot_{\text{pointwise}} I^{b*}}$ is still valid to use. Moreover, in order to accelerate computation speed, we also proposed a cylinder 0-1 phantom generated as $w_{\boldsymbol{r}}$. This way of implementation not only drastically decreases computation cost, but also provides flexibility of an adjustable basis to cover scan object in further interpolation.

3.2.3 Legendre Polynomial Basis

Legendre polynomials are used in many areas of mathematics, physics and engineering[11]. They have been well studied from a mathematical point of view. Legendre polynomials are the most general solution to Legendre's differential equation. A recursive definition of Legendre polynomials is as follows

$$\begin{aligned} l_0(x) &= 1 \\ l_1(x) &= x \\ l_{n+1}(x) &= \frac{(2n+1)x l_n(x) - n l_{n-1}(x)}{(n+1)} \end{aligned}$$

An important property of the Legendre polynomials is that they are orthogonal with respect to the L^2 inner product on a interval $-1 \leq x \leq 1$. Hence, any continuous function in the interval [-1, 1] can be expressed as a linear combination of Legendre polynomials,

$$f(x) = \sum_i a_i l_i(x)$$

In our application, the polynomial basis is expanded to multivariant basis,

$$p_m(\boldsymbol{r}) = l_i(x) l_j(y) l_k(z) \tag{3.7}$$

Consequently, a 3D continuous sensitivity profile can be expressed as a linear combination of Legendre polynomials,

$$S_c(\boldsymbol{r}) = \sum_m a_{m,c} p_m(\boldsymbol{r})$$

Thus, the sensitivity profile of size $M \times N \times L$ can be translated to a function between [-1,1] in x, y, z-axis by assuming $\frac{M}{2}$ pixels per unit length along x-axis, $\frac{N}{2}$ pixels per unit length along y-axis and, and $\frac{L}{2}$ pixels per unit length along z-axis. The entire image was fitted in the $2 \times 2 \times 2$ space around the origin to represent the whole image using Legendre polynomials.

3.3 Results and Discussion

3.3.1 Phantom Results

Based on the proposed sensitivity mapping scheme, a 3D sphere phantom was scanned using both the body coil and an 8-channel head coil with resolution $128 \times 128 \times 128$. Subsampling fully sampled body coil and head coil data generates a $26 \times 26 \times 26$ low resolution data set, which was used to fit polynomials. Three experiments were investigated to determine the proper model, polynomial basis, and order of polynomial basis to profile sensitivity. To evaluate the quality of our sensitivity mapping, the phantom image $I(\boldsymbol{r})$ was reconstructed with fully sampled head coils data $I_c^h(\boldsymbol{r})$ and interpolated sensitivity profiles $S_c(\boldsymbol{r})$ as follows,

$$I(\boldsymbol{r}) = \frac{\sum_c I_c^h(\boldsymbol{r}) S_c(\boldsymbol{r})^*}{\sum_c S_c(\boldsymbol{r}) S_c(\boldsymbol{r})^*} \tag{3.8}$$

Ordinary Polynomial Model vs. Rational Polynomial Model

In this set of experiments, the ordinary polynomial model Eq. 3.1 and rational polynomial model Eq. 3.3 were set up to fit the $26 \times 26 \times 26$ low resolution data set. At the same time, the orthonormal polynomial basis $\{p_m(\boldsymbol{r}) | p_m(\boldsymbol{r}) = x^i y^j z^k, -1 \leq x, y, z \leq 1, 0 \leq i + j + k \leq 7\}$ was used to fit sensitivity S_c in ordinary polynomial model and numerator S_p in rational polynomial model. And for the denominator S_q in rational polynomial model, the basis $\{p_m(\boldsymbol{r}) | p_m(\boldsymbol{r}) = x^i y^j z^k, -1 \leq x, y, z \leq 1, 0 \leq i + j + k \leq 4\}$ was chosen. Results are shown in Fig. 3.1 and Fig. 3.2.

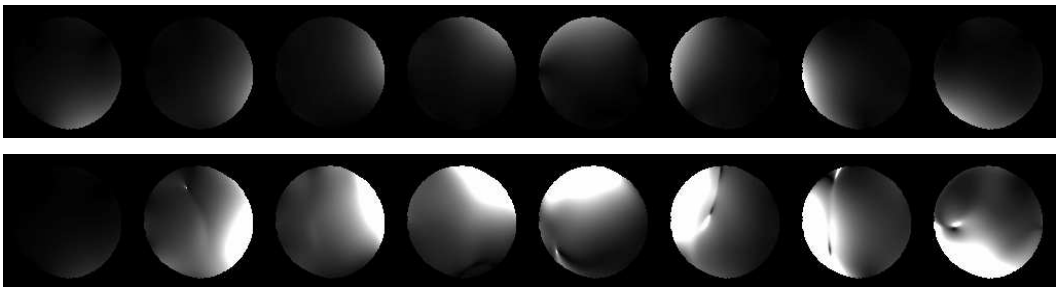

Figure 3.1: Interpolated Sensitivity in Different Models: upper row is from ordinary fitting model and lower row is from rational fitting model.

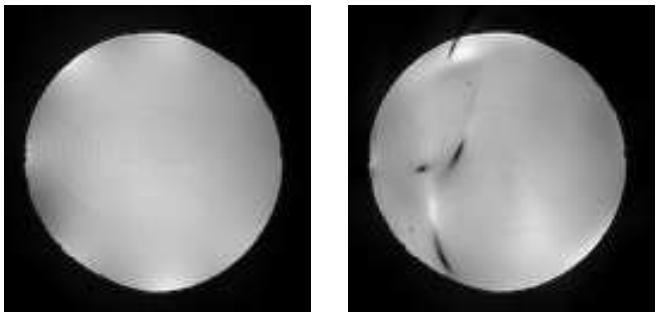

(a) (b)

Figure 3.2: Reconstructed Images in Different Models: (a) ordinary polynomial fitting model, (b) rational polynomial fitting model.

Polynomial Basis Selection

In order to choose a polynomial basis which is good enough to generate a smooth sensitivity map as well as relatively low in computation, we investigated four different polynomials, namely orthonormal polynomials, cylinder-weighted polynomials, body image-weighted polynomials, and Legendre polynomials. All of the above polynomials were generated up to order of 7 to fit $26 \times 26 \times 26$ low resolution data set using ordinary sensitivity fitting model. Results shown below are interpolated sensitivity at the resolution $100 \times 100 \times 100$.

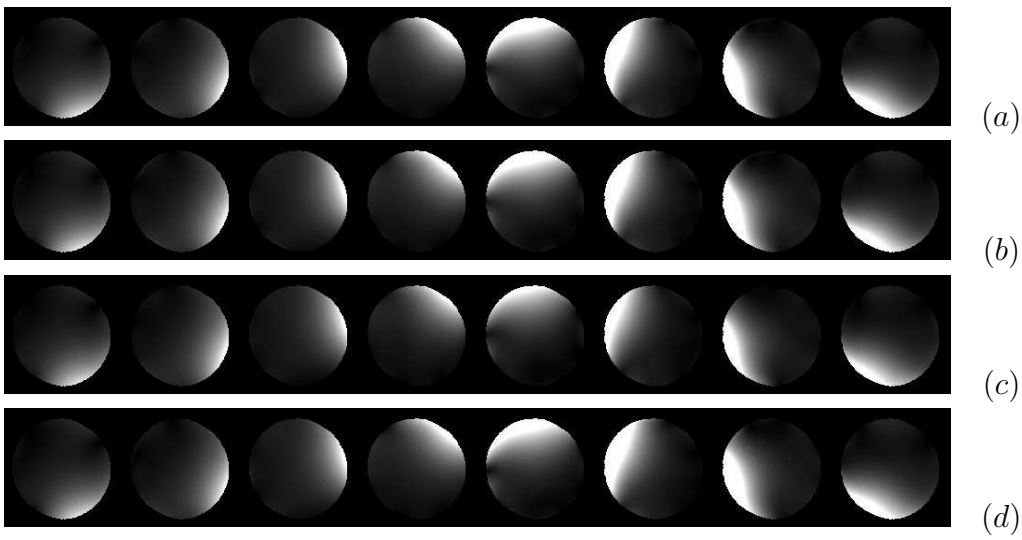

Figure 3.3: Sensitivity with Different Polynomial Bases: (a) orthogonal polynomial basis, (b) cylinder-weighted orthogonal polynomial basis, (c) body image-weighted orthogonal polynomial basis, (d) Legendre polynomial basis.

Polynomial Order Selection

Considering the order of polynomials might have an effect on sensitivity fitting, a comparison was undertaken among polynomials of order ranging from 6 to 9. The orthonormal polynomials and Legendre polynomials were chosen as the basis for this experiment. The same sphere phantom with low resolution data $26 \times 26 \times 26$ was fitted and $100 \times 100 \times 100$ high resolution sensitivity was generated by interpolation. Results are shown in Fig. 3.5 and computation time is listed in Table. 3.1.

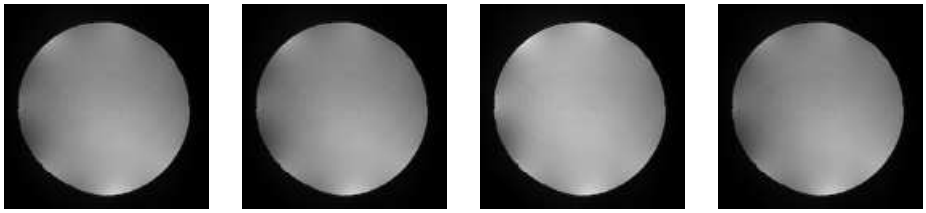

(a) (b) (c) (d)

Figure 3.4: Reconstructed Image with Different Polynomial Bases: (a) orthogonal polynomial basis, (b) cylinder-weighted orthogonal polynomial basis, (c) body image-weighted orthogonal polynomial basis, (d) Legendre polynomial basis.

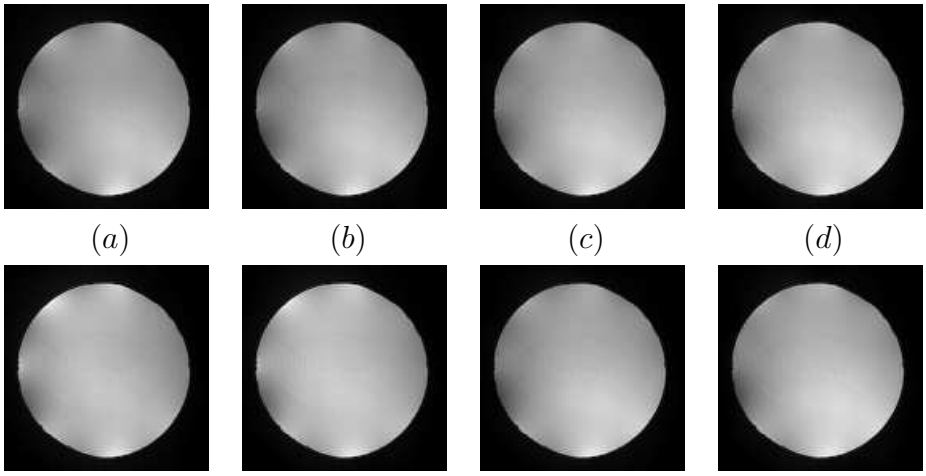

(a) (b) (c) (d)

(e) (f) (g) (h)

Figure 3.5: Reconstructed Image with Different Orders of Polynomial Basis:(a)-(d) Legendre polynomials of order 6 to 9 from right to left. (e)-(h) Orthonormal polynomials of order 6 to 9 from right to left.

Discussion

As a conclusion, although the rational polynomial model fits sensitivity of most FOV, there is region with unexpected extreme values. It is because

the objective function in Eq. 3.3 is not penalized when $S_{p,c}(\boldsymbol{r})$ and $S_{q,c}(\boldsymbol{r})$ go to 0. As a result, the discontinuity of the $S_c(\boldsymbol{r})$ shows up (see Figure 3.2). On the contrary, the ordinary model fits the low resolution pretty well and the generated sensitivity map is successfully used to reconstruct the images. Among different polynomial bases in experiments, Legendre polynomials gave the best sensitivity mapping results. Meanwhile, with increasing order of polynomials, Legendre polynomial basis demonstrates an improved error elimination, whereas orthonormal polynomial basis doesn't. In terms of computation cost, time of computing orthonormal polynomials increases drastically with respect to order and interpolated resolution, because of the complexity of Gram-Schmidt procedure. For k polynomial bases with n dimensionality, the cost of this computation is asymptotically $2nk^2$ floating point operations[2]. Although Legendre polynomials demonstrate faster computation comparing with orthonormal polynomial basis, the computation time is still not satisfactory, especially in high resolution interpolation.

In order to achieve higher computation performance in sensitivity profiling, we generated a set of polynomial basis with MAPLE in advance. As discussed above, the experiments with different polynomial basis demonstrate that although orthonormal polynomial bases cannot compete with Legendre polynomials in fitting sensitivity, the difference is small enough to assume they have equivalent performance in sensitivity mapping. Based on this assumption, we can easily generate a set of orthogonal polynomial basis in advance with any symbolic computation tool. Consequently, the computation time will efficiently decrease, see in Table 3.1. Moreover, to simplify MAPLE computation, the normalization in Gram-Schmidt process was omitted.

Table 3.1: Computation time with different polynomial orders (sec) using MATLAB R2010a installed on a 2.6GHz dual-core AMD Opteron processor.

Order	6	7	8	9
Legendre	137	153	256	434
Orthonormal	1659	1912	4020	7213
Orthogonal (MAPLE)	124	144	203	292

3.3.2 Brain Data Results

In addition to previous preliminary studies about polynomial properties and model efficiency, we applied the technique on brain image dataset. A relatively low resolution (64×64) 2D brain image data was acquired from both body coil and 8-channel head coil. In addition, images of the same object were collected by head coil at higher resolution, 400×400. The full reconstructed image is shown Fig. 3.6, which clearly shows that our approach successfully fixed the low signal area in the middle area which is caused by assumption body image is equivalent to square root of sum of surface coil signals, $I^b = \sqrt{\sum I^{h^2}}$. Moreover, with the polynomials which have already been generated in advance by MAPLE, computation time is significantly decreased.

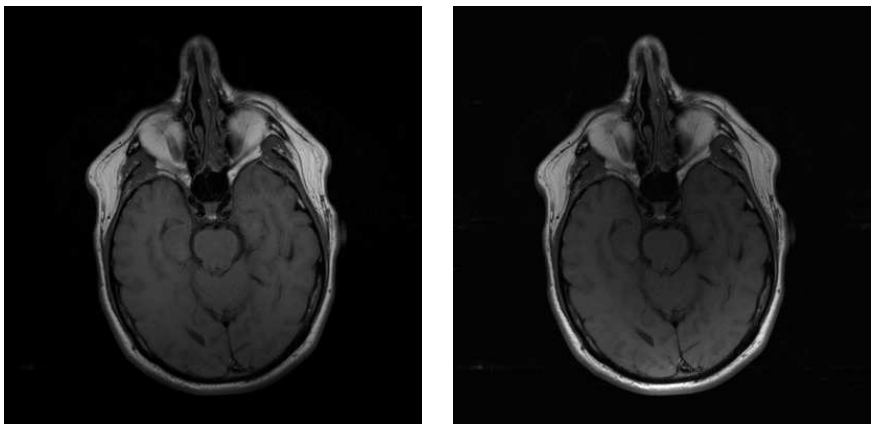

(a) (b)

Figure 3.6: (a) reconstructed brain image using the sensitivity profiling calculated from the proposed approach; (b) reconstructed brain image using the sensitivity calculated based on assumption that $\sqrt{\sum I^{h^2}}$ is body coil data.

Chapter 4

Undersampling Optimization

As mentioned in Chapter 2, SENSE imaging utilizes data redundancy from multiple detectors to decrease phase encoding steps. Consequently, scanning is accelerated based on the subsampling pattern in k-space. In this section, a nonlinear semi-definite model is designed to optimize the subsampling pattern. Meanwhile, the phantom shape is taken into consideration in the optimization procedure.

4.1 Semi-definite Optimization Model

Generally speaking, SENSE imaging procedure can be modeled as follows,

$$M_c = E_c \boldsymbol{\rho} + \boldsymbol{\epsilon}$$

where M_c is the measurements from the cth surface coil, E_c is the sensitivity encoding matrix of the surface coil, $\boldsymbol{\rho}$ is the image to be constructed, $\boldsymbol{\epsilon}$ is the system error which is caused by noises and inhomogeneity of magnetic field. Combination of signals from multiple detectors generates a large linear system representing the imaging process as shown below,

$$\begin{aligned} M &= E\boldsymbol{\rho} + \boldsymbol{\epsilon} && (4.1) \\ M &= (M_1, M_2, \cdots, M_c)^T && (4.2) \\ E &= (E_1, E_2, \cdots, E_c)^T && (4.3) \end{aligned}$$

Reconstructing image $\boldsymbol{\rho}$ from Eq. 4.1 is an inverse problem. To solve for the effect of noise on the $\boldsymbol{\rho}$ estimates, multiply both side of Eq. 4.1 by the adjoint, $E^* = \bar{E}^T$, and solve for $\boldsymbol{\rho}$,

$$E^* E \boldsymbol{\rho} = E^* M - E^* \boldsymbol{\epsilon} \tag{4.4}$$

Assuming that sufficient phase encoding have been collected to be able to reconstruct the peak amplitudes, E^*E is invertible, so we can write Eq. 4.4 as shown below,

$$\boldsymbol{\rho} = (E^*E)^{-1}E^*M - (E^*E)^{-1}E^*\boldsymbol{\epsilon} \tag{4.5}$$

where the first term is the estimation of $\boldsymbol{\rho}$ and the second term is the noise. The linear system used for the estimation of $(E^*E)^{-1}E^*$ is known as the Moore-Penrose pseudo-inverse. Eq. 4.5 shows the role of E in amplifying the noise. To reduce noise, we can maximize SNR in different ways, depending on whether we we are concerned with the reconstruction overall or with individual measurement. In this thesis, the worst-case SNR is chosen to be maximized, which corresponds to the minimum eigenvalue of E^*E.

[1] introduced a method of optimizing non-uniform sampling in multi-dimensional NMR with respect to expected noise. The same eigenvalue maximization approach using a semi-definite constraint can be adapted to the present problem. More specifically, maximizing the minimum eigenvalue of E^*E can be formulated as a semi-definte programming (SDP) problem, given undersampling parameters $\boldsymbol{r}_d$,

$$\max_{\boldsymbol{r}_d} \quad \lambda \tag{4.6}$$

$$s.t. \quad E^*E - \lambda I \succeq 0 \tag{4.7}$$

where $\succeq$ is a semi-definite inequality. The variable λ which is equal to the minimum eigenvalue of E^*E, is introduced to put the problem in the standard form. The effect of this inequality is to require the eigenvalues in Eq. 4.7 to be non-negative, which is equivalent to bounding the eigenvalues of E^*E below by λ. The practical importance of formulation the problem in this way is that there are a growing number of open-source or academically available solvers for SDP, which required a standard formulation as shown above.

4.2 Encoding Matrix Simplification

In Eq. 4.7, E is a linear system corresponding to encoding procedures in SENSE imaging. The structure of E depends on our undersampling scheme in k-space. In 3D Cartesian SENSE imaging, two gradient fields, perpendicular to the readout direction, are used for phase encoding. As a result, the optimization problem can be reduced to arbitrary 2D undersampling. For each phase encoding gradient, the corresponding sample point is denoted as

$\{\boldsymbol{k}_d | \boldsymbol{k}_d \in \mathbb{R}^2\}$. In the image domain, the undersampling vectors are denoted as $\{\boldsymbol{r}_{d1}, \boldsymbol{r}_{d2} | \boldsymbol{r}_{d1}, \boldsymbol{r}_{d2} \in \mathbb{R}^2\}$, which are the parameters to be optimized in this problem.

To optimize undersampling in the image domain we write the encoding matrix E in the same domain, as follows,

$$E(\boldsymbol{r}_{d1}, \boldsymbol{r}_{d2}) = \begin{pmatrix} V & & & \\ & V & & \\ & & \ddots & \\ & & & V \end{pmatrix} \begin{pmatrix} S_1 \\ S_2 \\ \vdots \\ S_c \end{pmatrix} \tag{4.8}$$

where S_c is the sensitivity matrix, the size of which depends on the resolution of the reconstructed image. V is the folding matrix which is determined by undersampling vectors $\boldsymbol{r}_{d1}$, $\boldsymbol{r}_{d2}$.

The dependence of the matrix size on the unfolding factor leads to a problem impossible to solve in practice. To overcome it, further assumptions were made, as follows,

- **Assumption 1**: the model is based on a $M \times N$ undersampling pattern, which means that in k-space subsampling, data is acquired approximately every M, N lines along each phase encoding direction. The corresponding image domain reveals each pixel has $MN - 1$ different points aliased with itself.

- **Assumption 2**: optimization is based on the point with the lowest SNR within the (unaliased) object. For most surface coil, the area is usually in the center of the object, corresponding position in our coordinates $\boldsymbol{r} = (0, 0)$.

Based on the above two assumptions, the size of V is fixed, given the lowest SNR point P_0, coordinated at $\boldsymbol{r}_0$, the aliased points set is $\{\boldsymbol{r} | \boldsymbol{r} = \boldsymbol{r}_0 \pm i\boldsymbol{r}_{d1} \pm j\boldsymbol{r}_{d2}, \boldsymbol{r}_0, \boldsymbol{r}_{d1}, \boldsymbol{r}_{d2} \in \mathbb{R}^2\, i \in \{0, \cdots, M-1\}, j \in \{0, \cdots, N-1\}\}$. Consequently, $E(\boldsymbol{r}_{d1}, \boldsymbol{r}_{d2})$ is simplified as follows,

$$E(\boldsymbol{r}_{d1}, \boldsymbol{r}_{d2}) = [\boldsymbol{s}_1(\boldsymbol{r}), \boldsymbol{s}_2(\boldsymbol{r}), \cdots, \boldsymbol{s}_c(\boldsymbol{r})]^T \tag{4.9}$$

where $\boldsymbol{s}_c(\boldsymbol{r})$ is a vector representing sensitivity from the cth surface coil at the location $\{\boldsymbol{r}\}$. The encoding matrix size for the lowest SNR point is $N_c \times MN$, where N_c represents the number of coils, M,N represents the base subsampling pattern in k-space.

4.3 Modified Model with Linear Constraints

As described above, the choice of the number of phase encodes M, N affects the quality of the reconstruction. Increasing M, N results in an increase of the rank of the matrix E, yielding pseudoinverses that are better conditioned. Consequently, the optimization problem Eq. 4.7 is expected to push $\boldsymbol{r}_{d1}$, $\boldsymbol{r}_{d2}$ as far out as possible to get a better conditioned matrix. However, in practice, this is not what happened. Given a point which is the aliasing point with the lowest SNR point P_0, if the point falls into the area where the object doesn't cover, this point should be eliminated from the aliasing set $\{\boldsymbol{r}\}$, because these points barely have information of the object.

To prevent points from falling outside of the object area, constraints are needed in addition to Eq. 4.7. In our design, 8 linear constraints $\{f_i(\boldsymbol{r})|f \in \mathbb{R}, i = 1, \cdots, 8\}$ were added to the semi-definite model. The 8 linear constraints give a hexagon area which covers the round scan object and constrain all the aliased points with P_0 inside. Although a nonlinear function can give a better constraint on object area, it is difficult to integrate nonlinear constraints into a standard SDP. From a practical point of view, most of the open-source semi-definite solvers or academically available solvers are unable to handle SDPs with nonlinear constraints. To sum up, the modified SDP model is shown as follows,

$$\max_{\boldsymbol{r}_d} \quad \lambda \tag{4.10}$$

$$s.t. \quad E^*E - \lambda I \succeq 0 \tag{4.11}$$

$$f_i(\boldsymbol{r}) \geq 0 \tag{4.12}$$

Chapter 5

Trust-Region Method

The model from Chapter 4 is a nonlinear semi-definite problem. Unfortunately, most of the open-source and academically available solvers are incapable to solve nonlinear SDPs. As an alternative, Taylor expansion is used to reformulate the problem to be a linear SDP problem and trust-region methods are applied to solve the problem iteratively. In this section, we will introduce the trust-region methods and their application to solve the semi-definite problem in Eq. 4.10

5.1 Trust-Region Method

Trust-region methods are iterative methods, which are widely used in nonlinear optimization problems[5]. In each iteration, a region Δ_k around the current iterate x_k is defined. Within the region Δ_k, the estimate model m_k is considered to be an adequate representation of the objective function f. Then the step p_k is chosen to be the approximate minimizer of the model m_k in this region. If a step p_k is not acceptable, they reduce the size of the region Δ_k and find a new minimizer.

The effectiveness of trust-region methods is mainly determined by the size of the trust-region Δ_k. If the region is too small, the algorithm misses an opportunity to take a substantial step that will move it much closer to the minimizer of the objective function. If too large, the minimizer of the model may be far from the minimizer of the objective function in the region, so the size of the region is needed to reduce and try again. In practical, the size of the region is chosen according to the performance of the algorithm, during previous iteration. If the model is consistently reliable, producing good steps

and accurately predicting the behavior of the objective function along these steps, the size of the trust-region may be increased to allow larger step to be taken. A failed step indicates that our model is an inadequate representation of the objective function over the current trust-region. After such a step, the size of the region should be reduced and try again[5].

One of the critical ingredients in a trust-region algorithm is the strategy for choosing the trust-region radius Δ_k. The choice is usually based on the agreement between the model function m_k and the objective function f at previous iterations. Given a step p_k, we define the ratio

$$\eta_k = \frac{f(x_k) - f(x_k + p_k)}{m_k(0) - m_k(p_k)}$$

the numerator is called the actual reduction, and the denominator is the predicted reduction, which is the reduction in f predicted by the model function. Since step p_k is obtained by minimizing the model $m_k(p_k)$ over a region that includes $p_k = 0$, the predicted reduction will always be nonnegative. Hence, if η_k is negative, the new objective value $f(x_k + p_k)$ is greater than the current values $f(x_k)$, so the step must be rejected. On the other hand, if η_k is close to 1, there is a good agreement between m_k and the function f over this step, so it is safe to expand the trust-region for the next iteration. If η_k is positive but significantly smaller than 1, we don't alter the trust-region, but if it is close to zero or negative, we shrink the trust region by reducing Δ_k at the next iteration[5].

5.2 SDP Reformulation

A standard SDP is defined as follows,

$$\min \quad \boldsymbol{c}^T \boldsymbol{x} \tag{5.1}$$

$$\text{s.t} \quad F(x) \succeq 0 \tag{5.2}$$

where

$$F(x) = F_0 + \sum_{i=1}^{m} x_i F_i \tag{5.3}$$

The problem data are the vector $\boldsymbol{c} \in \mathbb{R}^m$ and $m + 1$ symmetric matrices

$F_0, \cdots, F_m \in \mathbb{R}^{n\times n}$. The inequality sign in $F(x) \succeq 0$ means that $F(x)$ is positive semi-dfinite.

Instead of $\{F_i\}$ are constants in the standard form, the constraint matrix E^*E is a variable $\boldsymbol{r}_d$ dependent matrix. Each entry of the matrix is a quadratic function with respect to $\boldsymbol{r}_d^k = (r_1^k, r_2^k, r_3^k, r_4^k)^T$, where $r_1 = r_{xd1}^k, r_2 = r_{yd1}^k, r_3 = r_{xd2}^k, r_4 = r_{yd2}^k$. To reformulate Eq. 4.10 to the standard format as shown in Eq. 5.1, order of 1 Taylor-series expansion of E^*E is applied at $\boldsymbol{r}_d^k$, which is,

$$E^*E(\boldsymbol{r}_d) \triangleq E^*E^k + \sum_i \delta r_i \nabla E^* E_i^k \tag{5.4}$$

where

$$E^*E^k = E^*E|_{\boldsymbol{r}_d=\boldsymbol{r}_d^k} \tag{5.5}$$

$$\nabla E^*E_i^k = \frac{\partial E^*E}{\partial r_i}|_{\boldsymbol{r}_d=\boldsymbol{r}_d^k} \tag{5.6}$$

since Eq. 5.5 is only trusted within region Δ_k, a linear constraint is added on the SDP model, as shown below,

$$|\delta \boldsymbol{r}_d^k| \leq \Delta_k \tag{5.7}$$

Formulate the Eq. 5.7 in the matrix format as following,

$$\sum_i \delta r_i H_i + \Delta_k I \geq 0 \tag{5.8}$$

where

$$\begin{aligned} H_1 &= \begin{pmatrix} 1 & & & \\ & -1 & & \\ & & & \\ & & & \end{pmatrix} \quad H_2 = \begin{pmatrix} & & & \\ & 1 & & \\ & & -1 & \\ & & & \end{pmatrix} \\ H_3 &= \begin{pmatrix} & & & \\ & 1 & & \\ & & -1 & \\ & & & \end{pmatrix} \quad H_4 = \begin{pmatrix} & & & \\ & & & \\ & & 1 & \\ & & & -1 \end{pmatrix} \end{aligned} \tag{5.9}$$

As for the linear constraints $\{f_j(\boldsymbol{r}_d)\}$ in Eq. 4.10 can simply be reformulated as follows,

$$f_j(\boldsymbol{r}_d) = \sum_i g_{i,j}\delta r_i + c_j^k \tag{5.10}$$

where $g_{i,j}$ is a constant, which represents the coefficient of the corresponding variables in each constraint, c_i^k is a constant represents the constant term in linear constraint f_i at each iterate $\boldsymbol{r}_d^k$. In the matrix point of view, the linear constraints $\{f_i\}$ can be written as the following matrix format,

$$\sum_i \delta r_i G_i + C \geq 0 \tag{5.11}$$

where

$$G_i = \begin{pmatrix} g_{i,1} & & & \\ & g_{i,2} & & \\ & & \ddots & \\ & & & g_{i,8} \end{pmatrix} \quad C = \begin{pmatrix} c_1 & & & \\ & c_2 & & \\ & & \ddots & \\ & & & c_8 \end{pmatrix} \tag{5.12}$$

To sum up the above reformulation procedure, our final reformulated standard linear SDP model in each iterate $\boldsymbol{r}_d^k$ is shown as follows,

$$\begin{aligned} \max_{\delta \boldsymbol{r}_d^k} \quad & \lambda \\ s.t. \quad & F_0 + \textstyle\sum_{i=1}^4 \delta r_i F_i + \lambda F_5 \succeq 0 \end{aligned} \tag{5.13}$$

where

$$\begin{aligned} F_0 &= \begin{pmatrix} E^* E^k & & \\ & \Delta_k I & \\ & & C \end{pmatrix} \\ F_i &= \begin{pmatrix} \nabla E^* E_i^k & & \\ & H_i & \\ & & G_i \end{pmatrix}_{\{i=1\cdots 4\}} \\ F_5 &= \begin{pmatrix} I & & \\ & 0 & \\ & & 0 \end{pmatrix} \end{aligned}$$

In order to evaluate the step $\delta(r)_d^k$, the evaluating function is defined as follows,

$$\eta_k = \frac{f(\boldsymbol{r}_d^k) - f(\boldsymbol{r}_d^k + \delta\boldsymbol{r}_d^k)}{m(0) - m(\delta\boldsymbol{r}_d^k)} \tag{5.14}$$

where $m(\delta\boldsymbol{r}_d^k)$ is the minimum eigenvalue from Eq. 5.13, $f(\boldsymbol{r}_d^k)$ is the minimum eigenvalue of E^*E at $\boldsymbol{r}_d^k$.

With all the definitions and reformulations above, Eq. 5.13 can be solved following the trust-region methods with procedure shown as below,

Given $\hat{\Delta} \geq 0$,$\Delta_0 \in (0, \hat{\Delta})$:
for $k = 0, 1, 2, \cdots$
    Obtain $\delta\boldsymbol{r}_d^k$ by (approximately) solving Eq. 5.13
    Evaluate η_k from Eq. 5.14
    if $\eta_k < \frac{1}{4}$
        $\Delta_{k+1} = \frac{1}{\sqrt{2}}\Delta_k$
    else
        if $\eta_k > \frac{3}{4}$ and $||\delta\boldsymbol{r}_d^k|| = \Delta_k$
            $\Delta_{k+1} = \min(\sqrt{2}\Delta_k, \hat{\Delta})$
        else
            $\Delta_{k+1} = \Delta_k$
    if $\eta_k > \frac{1}{4}$
            $\boldsymbol{r}_d^{k+1} = \boldsymbol{r}_d^k + \delta\boldsymbol{r}_d^k$
    else
            $\boldsymbol{r}_d^{k+1} = \boldsymbol{r}_d^k$
end(for)

Chapter 6

Results

In this chapter, two sets of data were tested with our sensitivity profiling method and SDP model. Reconstructed images using optimally subsampled and conventional regularly subsampled k-space data are compared. In addition, numerical estimates for noise amplification are shown and validated against acquired images.

6.1 Phantom Simulation

In this simulation, a $100 \times 100 \times 200$ 3D data was acquired from an 8 channel head coil, of which the readout direction has resolution 200. The sensitivity profile was estimated based on a separate $50 \times 50 \times 50$ lower resolution dataset using an order-7, orthogonal-polynomial basis. The SDP model was set up based on one plane within the volume data perpendicular to the readout direction. The polynomial sensitivities were evaluated at in-plane voxels for the SDP problem, as well as image reconstruction.

Assuming that the centre of the FOV has the lowest SNR, two undersampling patterns were investigated on this dataset. One was a pattern with 6 points aliased with the centre point (case 1), the other had 4 aliased points (case 2). Linear constraints to keep the aliasing points with an overestimate of the phantom area were used, see in Figure 6.1$(a)(e)$.

The nonlinear, semi-definite optimization problem was solved in MATLAB using the solver SeDuMi_1.2.1, using the iterative trust-region method. In both of the cases, undersampling vectors were successfully optimized and presented a significant numerical improvement in noise amplification and stability

(as measured by the condition number) of reconstruction, see in Table 6.1.

Table 6.1: Numerical Result of Optimal Undersampling Vectors

	Minimum Eigenvalue		Condition Number of E		Data
	Initial	Optimal	Initial	Optimal	Acquisition
case 1	0.0442	0.9040	121.88	24.58	8.50%
case 2	2.2945	6.1139	12.95	8.56	11.68%

Based on the definition of the Fourier transform and the reciprocal principle, we converted the optimal undersampling vectors $\boldsymbol{r}_{d1}, \boldsymbol{r}_{d2}$ in the image domain to the corresponding undersampling vectors in k-space $\boldsymbol{r}_{k1}, \boldsymbol{r}_{k2}$, see in Appendix A. Since $\boldsymbol{r}_{k1}, \boldsymbol{r}_{k2}$ were not integers, we rounded the k-space positions to the nearest point on the normally sampled grid. In addition, the centre of k-space was densely sampled within a 10×10 square to preserve the contrast information. Based on these optimally sampled k-space data, images were successfully reconstructed, see in Figure 6.1.

Moreover, in order to compare our optimal sampling patterns with regular sampling pattern, a simulation of regular undersampling pattern 3×4 was used to collect k-space data. The same densely sample was taken in the centre of k-space, the amount of data acquired in total is 9.30%, similar to the case 1 data (8.50%). The same reconstruction procedure was applied on this data set. The reconstructed results is shown in Figure 6.2.

In the above results, it is demonstrated that the optimal subsampling pattern did a better job in image reconstruction and noise elimination. The amount of noise in the first case (7-fold aliasing) is 3.52×10^6, compared with 3.78×10^6 for the regular 3×4 sampling pattern. However, it is surprising that the 7-folded pattern produces a better image reconstruction than that of the 5-folded pattern, even though less data was used in the reconstruction. This is probably a result of rounding the optimal sample spacing to integer spacing in order to use a fully-acquired data set. Consequently, the sampling pattern after rounding was not the optimal any more and reconstruction performance cannot be expected to be of the same quality. This probably also explains why the optimal sampling pattern did not show significantly less noise amplification compared with regular subsampling. To investigate the effect of rounding in k-space on reconstruction, another phantom with larger FOV was acquired,

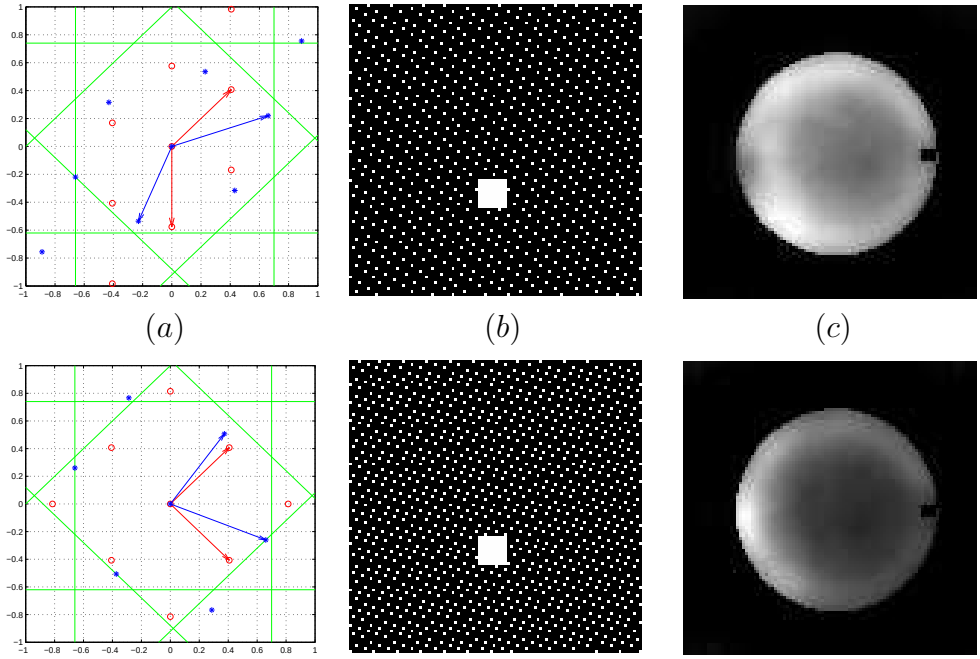

(a) (b) (c)

(d) (e) (f)

Figure 6.1: Optimal undersampling patterns in image space (a,d), and k-space (b,e) and reconstructed images (c,f). Red arrows show initial aliasing vectors; blue arrows show optimal aliasing vectors pattern; red dots show the initial aliased point set; blue dots show optimal aliased sets; green lines are the linear constraints in the SDP model. Case 1: (a,b,c). Case 2: (d,e,f).

and will be analysed in the next section.

6.2 Phantom Simulation with Larger FOV

In this section, a set of 2D phantom data with resolution 512×1024 was collected with a FOV 16 times larger than that necessary for the reconstructed image (128×256). Each direction of the k-space data had 4 times bigger FOV compared to the object. This allowed us to round optimal sample points in k-space to the nearest multiple of 0.25, rather than to integer points. Similarly

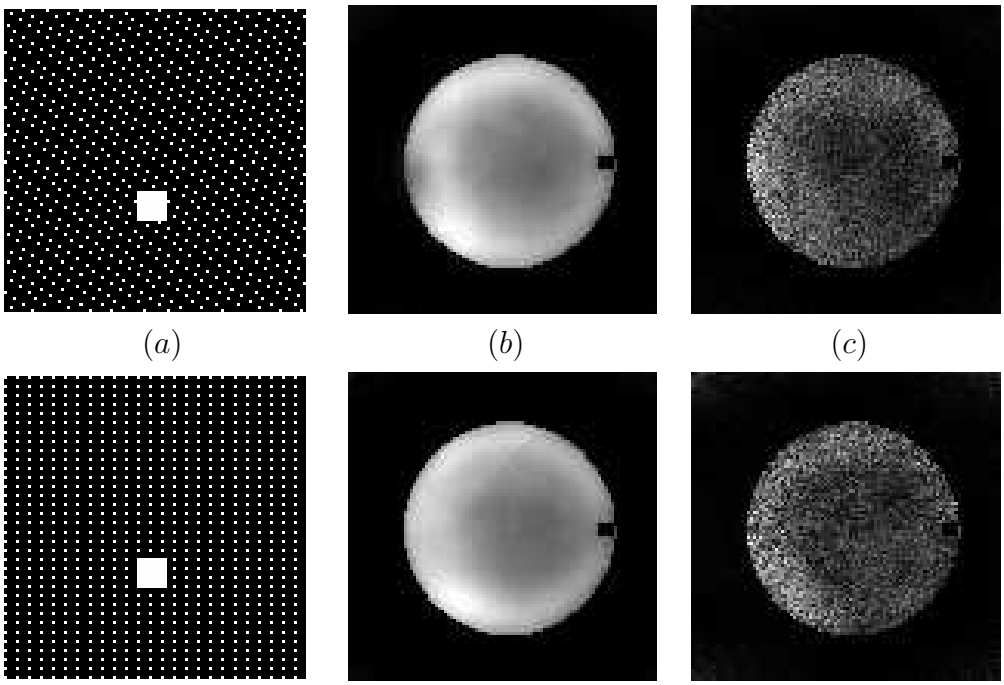

(a) (b) (c)

(d) (e) (f)

Figure 6.2: Rounded optimal (a) and regular (e) sampling patterns; corresponding reconstructed images without (b,e), and with (c,f) additional noise.

to the previous simulation, two initial undersampling patterns were investigated in the SDP model. The same solver was used to solve this problem. Optimal undersampling patterns were found in both cases; see in Table 6.2. Reconstructed images based on these patterns are shown in Figure 6.3

Table 6.2: Numerical Result of Optimal Undersampling Vector

	Minimum Eigenvalue		Condition Number of E		Data Acquisition
	Initial	Optimal	Initial	Optimal	
case3	0.0016	0.0054	424.71	222.23	12.32%
case4	0.0008	0.0046	562.44	239.69	13.45%

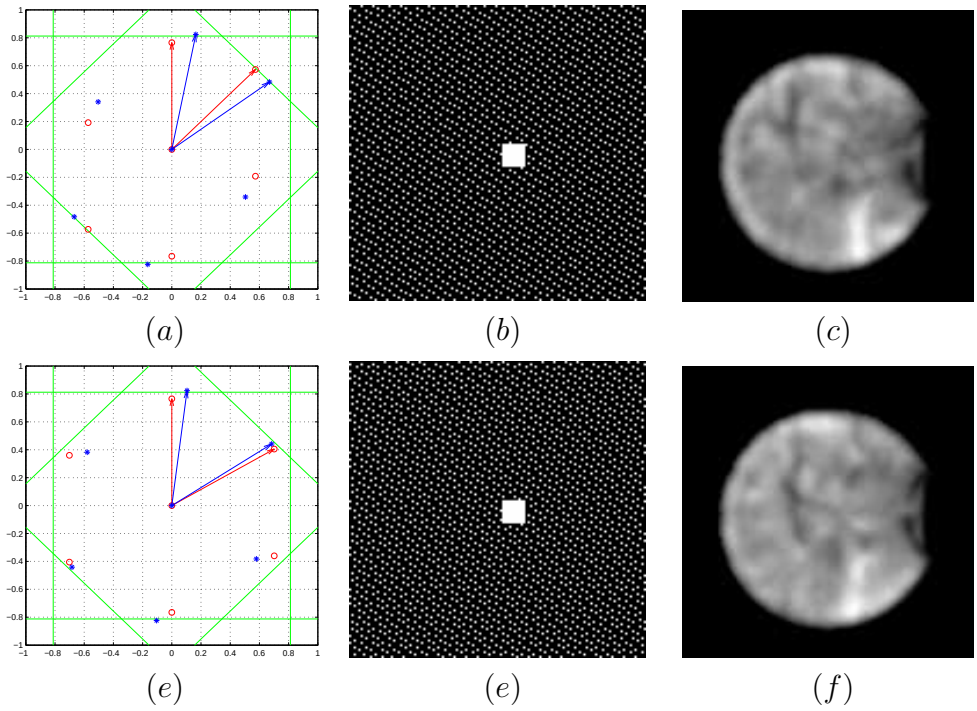

Figure 6.3: Optimal undersampling patterns in image space (a,d), and k-space (b,e) and reconstructed images (c,f), using 4X FOV data to reduce the loss of efficiency from rounding. Red arrows show initial aliasing vectors; blue arrows show optimal aliasing vectors pattern; red dots show the initial aliased point set; blue dots show optimal aliased sets; green lines are the linear constraints in the SDP model. Case 3: (a,b,c). Case 4: (d,e,f).

We also compare our optimal subsampling pattern with conventional subsampling, using a similar amount of data in k-space. In this set of simulations, case 4 was chosen to compare with 4×4 regular subsampling. In case 4, the amount of data collected to reconstruct image is 13.45% of the full k-space data, versus 11.80% for regular subsampling. The same reconstruction was applied on both sets of data. The reconstructed images in Figure 6.4, demonstrate that the optimal undersampling pattern provides better image recovery. To investigate the noise amplification effects of the optimal and regular subsampling patterns, different levels of artificial noise were added on the k-space data. Given the noise with mean 0 and deviation $a\%$, which $a\%$ means the

$a\%$ of the maximum energy in k-space data. Noise of levels 1%, 5%, 20% were added to the the k-space data.

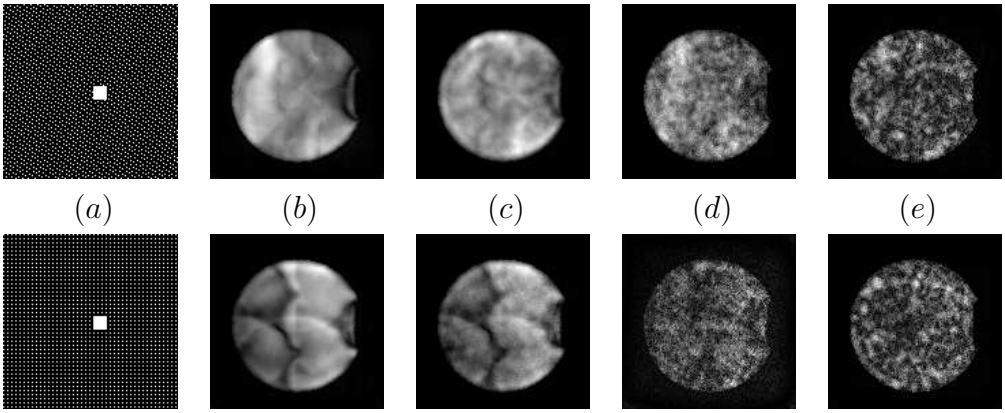

(a) (b) (c) (d) (e)

(f) (g) (h) (i) (j)

Figure 6.4: Reconstructed Image with Different Levels of Noise: the upper row is based on the optimal subsampling pattern; the lower on the regular subsampling pattern. (a)(f) undersampling pattern in k-space, (b)(g) without noise, (c)(h) 1% noise, (d)(i) 5% noise, (e)(j) 20% noise.

We investigated the reconstruction errors with respect to different levels of noise in measurements, see in Figure 6.5. The optimal subsampling pattern results in less noise amplification during image reconstruction.

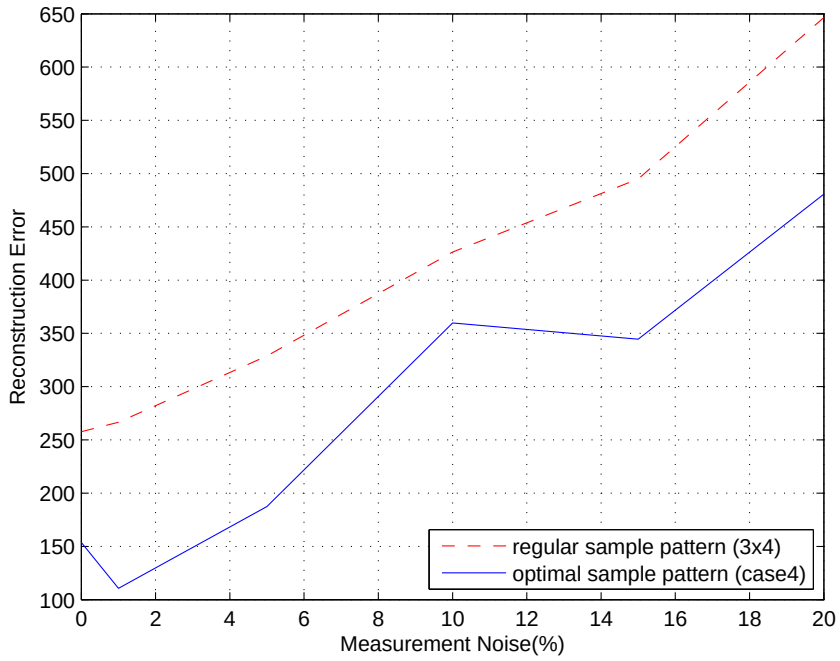

Figure 6.5: Reconstruction errors as a function of added noise.

Chapter 7

Conclusion

In this thesis, we have presented an efficient scheme for approximating sensitivity profiles with polynomials in order to optimize the undersampling pattern used in SENSE imaging. We have demonstrated numerically the improvement for system stability and noise reduction.

7.1 Sensitivity Profiling

We have investigated polynomial fitting based methods in sensitivity estimation in order to get accurate continuous sensitivity mappings for an SDP optimization problem and SENSE reconstruction. This approach is easily adapted to arbitrary planes and/or volumes, and is computationally inexpensive.

Moreover, there are still a wide range of factors that might improve the sensitivity mapping which need to be investigated. Since our sensitivity profiling method is only fitting the regularly sampled low resolution dataset, further research might investigate the influence of non-uniformly sampled low resolution datasets on sensitivity mapping. Moreover, customizing different polynomial bases for each channel of head coil might allow lower order of polynomials for each set, which might accelerate the fitting time. In addition, as for our rational polynomial fitting model, different solving approaches might lead to better results, for example, using a Gauss-Seidel approach solving the numerator and denominator polynomial iteratively.

7.2 SDP Model

We have shown that the SDP model can consistently improve the theoretical worst-case expected noise amplification caused by SENSE undersampled image reconstruction. The experimental validation of this expected improvement was limited by the available phased-array coil and scan software limitations on the pattern of acquired phase encoded lines and effective field of view. Nevertheless, the images reconstructed from optimized sampling patterns showed a marked reduction in aliasing and noise amplification, with noise amplification being measured by adding additional similuated noise to acquired k-space data.

In the future, it is important that these results be reproduced with more finely controlled phase encode postions and with higher multiples of coils.

Appendix A

Relation of Transformations Between Image Domain and K-space

Given a linear transformation C

$$\tilde{\boldsymbol{x}} = C\boldsymbol{x}$$

We are looking for the corresponding transformation in k-space,

$$\tilde{\boldsymbol{k}} = B\boldsymbol{k}$$

Based the definition of Fourier tranformation,

$$\rho(\boldsymbol{x}) = \int_{\mathbf{R}^3} \hat{\rho}(\boldsymbol{k}) e^{i\boldsymbol{x}^T\boldsymbol{k}} d\boldsymbol{k}$$

the Fourier transformation based on the translated basis,

$$\begin{aligned} \rho(\boldsymbol{x}) &= \int_{\mathbf{R}^3} \hat{\rho}(\boldsymbol{k}) e^{i\boldsymbol{x}^T\boldsymbol{k}} d\boldsymbol{k} && \text{(A.1)} \\ &= \int_{\mathbf{R}^3} \hat{\rho}(\boldsymbol{k}) e^{i(C^{-1}\tilde{\boldsymbol{x}})^T\boldsymbol{k}} d\boldsymbol{k} && \text{(A.2)} \\ &= \int_{\mathbf{R}^3} \hat{\rho}(\boldsymbol{k}) e^{i\tilde{\boldsymbol{x}}^T(C^{-1})^T\boldsymbol{k}} d\boldsymbol{k} && \text{(A.3)} \end{aligned}$$

Substitute $\tilde{\boldsymbol{k}} = (C^{-1})^T\boldsymbol{k}$ in A.3,

$$\rho(\boldsymbol{x}) = \int_{\mathbf{R}^3} \hat{\rho}(\boldsymbol{k}) e^{i\tilde{\boldsymbol{x}}^T\tilde{\boldsymbol{k}}} dC^T\boldsymbol{k}$$

it is clearly see that the translation in k-space is as follows,

$$B = (C^{-1})^T$$

.

Bibliography

[1] Christopher Kumar Anand, Alex D. Bain, and Anuroop Sharma. Optimized sampling patterns for multidimensional t2 experiments. *Journal of Magnetic Resonance*, 197(1):63 – 70, 2009.

[2] Gene H. (Gene Howard) Golub. *Matrix computations*. Johns Hopkins University Press, 3nd edition edition, 1996.

[3] Christopher J. Hardy, Robert D. Darrow, Manojkumar Saranathan, Randy O. Giaquinto, Yudong Zhu, Charles L. Dumoulin, and Paul A. Bottomley. Large field-of-view real-time mri with a 32-channel system. *Magnetic Resonance in Medicine*, 52(4):878–884, 2004.

[4] RobinM. Heidemann, zkan zsarlak, PaulM. Parizel, Johan Michiels, Berthold Kiefer, Vladimir Jellus, Mathias Mller, Felix Breuer, Martin Blaimer, MarkA. Griswold, and PeterM. Jakob. A brief review of parallel magnetic resonance imaging. *European Radiology*, 13:2323–2337, 2003. 10.1007/s00330-003-1992-7.

[5] Stephen J. Wright Jorge Nocedal. *Numerical Optimization*. Springer, 2nd edition edition, 2000.

[6] Yi-Hsuan Kao. The principles of magnetic resonance imaging, 2001.

[7] Walid E. Kyriakos, Lawrence P. Panych, Daniel F. Kacher, Carl-Fredrick Westin, Sumi M. Bao, Robert V. Mulkern, and Ferenc A. Jolesz. Sensitivity profiles from an array of coils for encoding and reconstruction in parallel (space rip). *Magnetic Resonance in Medicine*, 44(2):301–308, 2000.

[8] David J Larkman and Rita G Nunes. Parallel magneticc resonance imaging. *Physics in Medicine and Biology*, 52(7):R15–55, 2007.

[9] Zhi-Pei Liang, Paul C. Lauterbur Lauterbur, IEEE Engineering in Medicine, and Biology Society. *Principles of Magnetic Resonance Imaging: A Signal Processing Perspective*. SPIE Optical Engineering Press, illustrated edition, 2000.

[10] Patricia Nol, Roland Bammer, Caroline Reinhold, and Masoom A. Haider. Parallel imaging artifacts in body magnetic resonance imaging. *Canadian Association of Radiologists Journal*, 60(2):91 – 98, 2009.

[11] Sankaranarayanan Department Of and A. C. Sankaranarayanan. Image browsing using legendre polynomials and wavelets, 2002.

[12] Klaas P. Pruessmann. Encoding and reconstruction in parallel mri. *NMR in Biomedicine*, 19(3):288–299, 2006.

[13] Klaas P. Pruessmann, Markus Weiger, and Peter Boesiger. Sensitivity encoded cardiac mri. *Journal of Cardiovascular Magnetic Resonance*, 3(1):1–9, 2001.

[14] Klaas P. Pruessmann, Markus Weiger, Markus B. Scheidegger, and Peter Boesiger. Sense: Sensitivity encoding for fast mri. *Magnetic Resonance in Medicine*, 42(5):952–962, 1999.

[15] J. B. Ra and C. Y. Rim. Fast imaging using subencoding data sets from multiple detectors. *Magnetic resonance in medicine*, 30(1):142–145, 1993.

[16] Jun Shen and Yun Xiang. High fidelity magnetic resonance imaging by frequency sweep encoding and fourier decoding. *Journal of Magnetic Resonance*, 204(2):200 – 207, 2010.

[17] Johan S. van den Brink, Yuji Watanabe, Christiane K. Kuhl, Taylor Chung, Raja Muthupillai, Marc Van Cauteren, Kei Yamada, Steven Dymarkowski, Jan Bogaert, Jeff H. Maki, Celso Matos, Jan W. Casselman, and Romhild M. Hoogeveen. Implications of sense mr in routine clinical practice. *European Journal of Radiology*, 46(1):3 – 27, 2003.

[18] David O. Walsh, Arthur F. Gmitro, and Michael W. Marcellin. Adaptive reconstruction of phased array mr imagery. *Magnetic Resonance in Medicine*, 43(5):682–690, 2000.